Check for updates

Mg–CO2 Batteries

Boosted Mg–CO2 Batteries by Amine-Mediated CO2 Capture Chemistry and Mg2+-Conducting Solid-electrolyte Interphases

Chengxin Peng[+], Linlin Xue[+], Zhengfei Zhao, Longyuan Guo, Chenyue Zhang,*
Aoxuan Wang,* Jianfeng Mao, Shixue Dou, and Zaiping Guo*

Abstract: Mg–CO2 battery has been considered as an ideal system for energy conversion and CO2 fixation. However, its practical application is significantly limited by the poor reversibility and sluggish kinetics of CO2 cathode and Mg anode. Here, a new amine mediated chemistry strategy is proposed to realize a highly reversible and high-rate Mg–CO2 battery in conventional electrolyte. Judiciously combined experimental characterization and theoretical computation unveiled that the introduced amine could simultaneously modify the reactant state of CO2 and Mg^{2+} to accelerate CO2 cathodic reactions on the thermodynamic-kinetic levels and facilitate the formation of Mg^{2+}-conductive solid-electrolyte interphase (SEI) to enable highly reversible Mg anode. As a result, the Mg–CO2 battery exhibits boosted stable cyclability (70 cycles, more than 400 h at 200 mA g^{-1}) and high-rate capability (from 100 to 2000 mA g^{-1} with 1.5 V overpotential) even at $-15\,°C$. This work opens a newly promising avenue for advanced metal-CO2 batteries.

[*] C. Peng,[+] S. Dou
School of Materials and chemistry, Institute of Energy Materials Science, University of Shanghai Science and Technology
Shanghai 200093 (China)

L. Xue,[+] Z. Zhao, L. Guo, C. Zhang, A. Wang
Key Laboratory for Green Chemical Technology of Ministry of Education, School of Chemical Engineering and Technology, Tianjin University
Tianjin 300072 (China)
E-mail: chenyuezhang@tju.edu.cn
        aoxuanwang@tju.edu.cn

A. Wang
Key Laboratory of Advanced Energy Materials Chemistry (Ministry of Education), College of Chemistry, Nankai University
Tianjin 300071 (China)

J. Mao, Z. Guo
School of Chemical Engineering, The University of Adelaide
Adelaide, SA 5005 (Australia)
E-mail: zaiping.guo@adelaide.edu.au

[+] These authors contributed equally to this work.

Introduction

Due to the increasingly severe environmental pollution and global warming, clean fixation, conversion and utilization of the greenhouse gas-CO2 have become one of the most prevalent and pressing research topics for achieving sustainable development.[1] Among all the proposed systems to reduce CO2 emission, rechargeable metal-CO2 batteries have been considered as a promising strategy for effective CO2 reduction with few pollutions, which would, in turn, provide renewable energy for further fixation of CO2.[2] According to the type of anodes, metal-CO2 batteries are mainly divided into Li–CO2, Na–CO2, K–CO2, Mg–CO2, Zn–CO2, and Al–CO2 systems.[3] However, the high activity, high cost or dendrite nature may hinder the practical development the Li/Na/K–CO2 batteries.[4] Zn–CO2 and Al–CO2 are relatively low cost and low reactivity, but always suffer from the extremely low discharge voltage or high overpotential due to the inherently higher electric density and electrode potential of Zn and Al metal anodes (-0.76 V *vs.* Standard Hydrogen Electrode (SHE) and -1.66 V *vs.* SHE, respectively).[5–7] With the safety and economy in mind, Mg metal has been considered as an ideal anode for metal-CO2 battery system due to its unique features, i.e. relatively low-reduction potential (-2.37 V *vs.* SHE), high-volumetric capacity (3832 mAh cm^{-3}), dendrite-free nature at moderate current density and abundant reserves (2.9 %).[8,9] Matched with nonaqueous and cost-effective conventional electrolytes, Mg–CO2 battery exhibits tremendous promise for carbon utilization for efficient energy storage and conversion.

However, the nonaqueous rechargeable Mg–CO2 batteries are still infant with practical problems of high polarization, limited cycle current and/or delivery capacity. It would, actually, come down to two impediments: 1) Poor reversibility. Carbonate, MgCO3 in Mg–CO2 system specifically, considered as the final discharge product for the CO2 reduction reaction (CO2RR), is insulating and almost indecomposable.[10,11] It will thus accumulate on cathode, increasing the interfacial impedance and bruising the CO2 evolution reaction (CO2ER) upon recharge. In addition, the passivation of Mg anode in conventional electrolytes of course exacerbates the irreversibility further, leading to irreversible Mg–CO2 battery with a large overpotential and poor cycling performance. 2) Sluggish kinetics. Besides the acknowledged barriers for the cathodes including difficult de-solvation at cathode-electrolyte interface and sluggish Mg^{2+} diffusion within cathodes,[12] the kinetics of CO2RR

and CO_2ER at cathode are also hindered by the poor compatibility of ternary-phase interface, difficult breakage of C=O bonds and incomplete decomposition of discharge products.[13] As a result, $Mg–CO_2$ batteries often have the problems of deficient cycle current, limited capacity and fast capacity decay. Significant efforts like structural cathodes,[14] designed catalysts,[15,16] and reaction mediators,[17,18] *etc.*, have been devoted to improve interfacial contacts, drive CO_2 reduction or facilitate discharge product decomposition. However, due to the intrinsic properties of strong polarization and multi-electron transfer in $Mg–CO_2$ system, these reported strategies can hardly care the cathodic reversibility and kinetics simultaneously, together with the anode reversibility. Liquid amines, on the one hand, have been confirmed for avoiding passivation on Mg anode via the regulation of solvation structure and the anode interphase.[19,20] On the other hand, this motif have also been studied abundantly for activating electrochemical CO_2 conversion via chemical capturing.[21,22] Therefore, it is expected to adopt liquid amines to solve the notorious problems in $Mg–CO_2$ batteries.

Here we propose a "kill two birds with one stone" strategy to realize a highly reversible and high-rate $Mg–CO_2$ battery in conventional electrolyte via liquid 1, 3-propylene amine (PDA) medium chemistry approach (Figure 1a). By chemisorbing CO_2 and tailoring Mg^{2+} solvation coordination, the introduction of PDA can benefit for both cathode and anode. For cathodic reaction, PDA could improve the compatibility of multiphase interface, facilitate fast Mg^{2+} desolvation and diffusion, reduce the barrier of CO_2RR, render the formation of decomposable discharge product–MgC_2O_4, and in turn, enhance the kinetics of
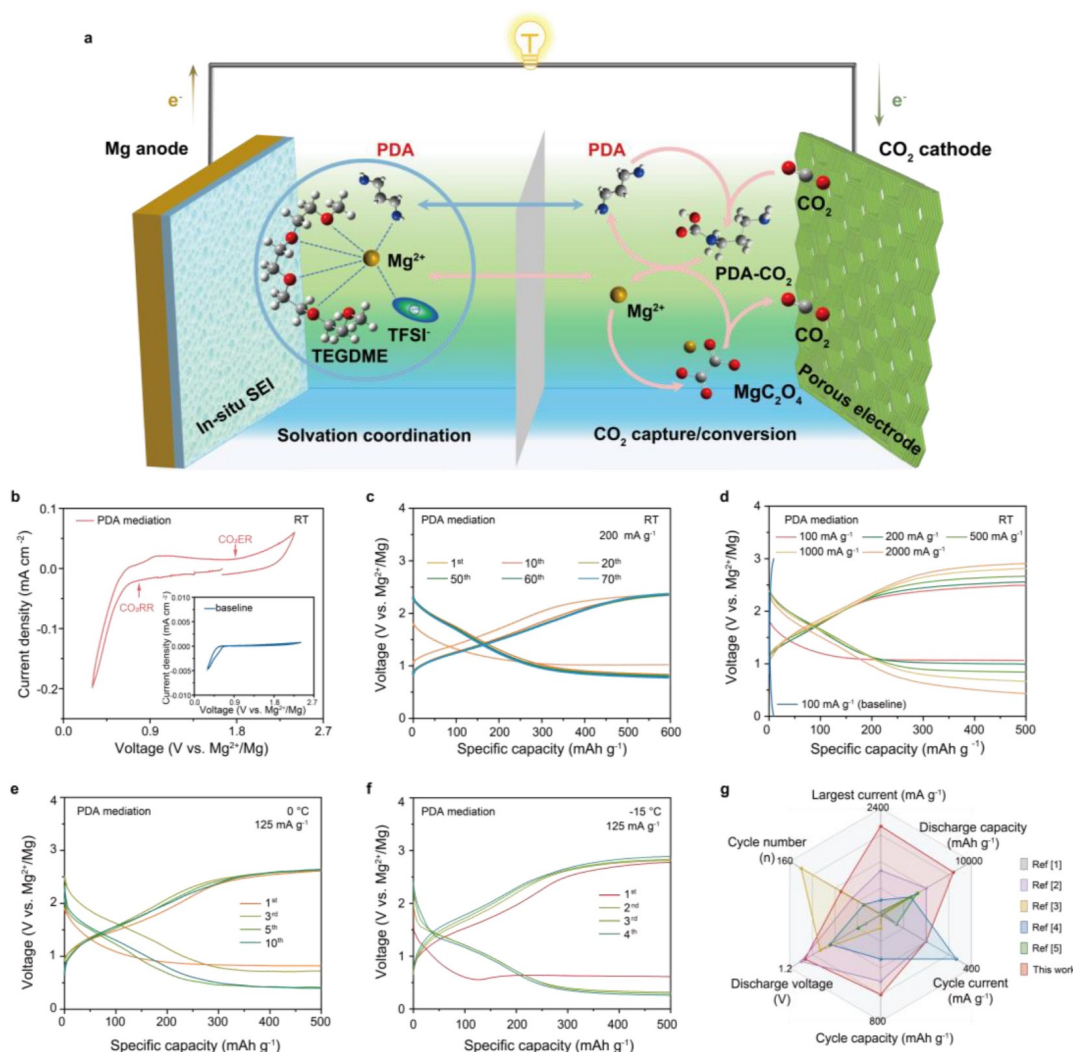

Figure 1. Electrochemical performance of Mg-CO_2 battery promoted by PDA chemistry. a) Schematic diagram of a $Mg–CO_2$ battery with PDA additive as bifunctional medium. b) CV curves of $Mg–CO_2$ batteries with PDA additive from 0.3 to 2.4 V at a scan rate of 0.2 mV s^{-1}. Inset: corresponding curve in baseline electrolyte. Selected discharge/charge cycles of $Mg–CO_2$ batteries with PDA mediation c) at 200 mA g^{-1} with a capacity of 600 mAh g^{-1}, e) at 125 mA g^{-1} with a capacity of 500 mAh g^{-1} under 0 °C and f) −15 °C. d) Rate performance under different current densities of $Mg–CO_2$ battery with PDA mediation, and discharge/charge cycle of $Mg–CO_2$ batteries without PDA mediation at 100 mA g^{-1}. g) Electrochemical performance comparison of multivalent metal-CO_2 batteries in nonaqueous electrolyte.

$CO_2ER.$[13,23] For anodic reaction, PDA induces the in situ formation of Mg^{2+}-conductive solid electrolyte interphase (SEI), enabling highly reversible Mg plating/stripping. Therefore, with the promotion of PDA medium, a highly reversible Mg–CO_2 battery with lifespan of over 400 h at 200 mA g^{-1} and superior rate performance from 100 to 2000 mA g^{-1} could be obtained in 0.25 M $Mg(TFSI)_2$-TEGDME electrolyte. Importantly, the system could also operate normally under low temperature of 0 °C or −15 °C, demonstrating the high CO_2 utilization ability and potential prospect of Mg–CO_2 batteries. The demonstrated amine-mediated chemistry strategy for promoted CO_2 capture and conversion provides a new avenue for developing high-performance metal-CO_2 batteries.

Results and Discussion

The Mg–CO_2 battery was composed of Mg metal as anode and nitrogen-doped carbon nanotubes (N-CNTs) as catalytic cathode. The actual assembled cell and the corresponding schematic diagram were displayed in Figure S1. 0.25 M $Mg(TFSI)_2$ in TEGDME (G4) was used as the baseline electrolyte for its chemical stability and commercial accessibility. 10 *wt*% PDA added in electrolyte was chosen as the optimal concentration according to the polarization and cyclic voltammetry (CV) tests for Mg anode (Figure S2). In this case, the CV curve of Mg–CO_2 system with PDA electrolyte exhibits remarkable CO_2RR (0.8 V) and CO_2ER (1.8 V) peaks with large current response, demonstrating the efficient CO_2 conversion involves in the electrochemical reactions. In contrast, without PDA, Mg–CO_2 battery operates irreversibly, as evidenced by the extremely low current response shown in inset CV curve (Figure 1b). Due to the reversible anode and promoted cathode reactions, the PDA-mediated Mg–CO_2 battery could maintain stable cycling for 70 cycles at 200 mA g^{-1} with a specific capacity of 600 mAh g^{-1} (Figure 1c), and display a lifespan over 400 h with overpotential from 1.3 to 1.5 V (Figure S3). Increasing the cycling capacity to 1000 mAh g^{-1}, the battery could still operate for 40 cycles at 200 mA g^{-1} without pronounced overpotential build-up (Figure S4). Moreover, superior rate performance could be also achieved with stable voltage plateaus at current densities from 100 to 2000 mA g^{-1}. In sharp contrast, Mg–CO_2 battery without PDA fails with extremely high overpotential and rapid capacity decay (Figure 1d, Figure S5). The promoted kinetics by PDA mediation can be further evidenced by the stable cycling of the batteries even under low temperature of 0 °C and −15 °C (Figure 1e–f, Figure S6), as well as the deep utilization of CO_2 which is reflected through the high discharge capacity of 4 mAh when Mg–CO_2 with PDA behaves as primary battery (Figure S7). The above batteries could also output a stable voltage to power a light-emitting diode (LED), further manifesting its practical feasibility. Considering both the long-term cycling and rate performance, the rechargeable Mg–CO_2 battery with PDA in our work have reached the highest level compared previous related literatures (Figure 1g and Table S5).

To understand the excellent performance of PDA-mediated Mg–CO_2 cycling, the cathodic reaction pathway behind the CO_2 conversion reaction is identified. After discharge process, as evidenced by scanning electron microscopy (SEM), spherical particles with only ≈100 nm in size were deposited on the interior and surface of porous N-CNTs mats cathodes, with Mg, C and O elements distributed evenly. The small particles, with short charge transfer pathways and exposed large surface areas, could be almost wholly reversible during subsequent recharge processes (Figure 2a, Figure S8–9). X-ray diffraction patterns (XRD) determined the main discharge product species is MgC_2O_4 (PDF#26–1222), whose peaks disappeared during charge process, corresponding well with the recovered cathode in SEM images (Figure 2b). Raman spectra also support the results. As depicted in Figure 2c, a new peak assigned to $C_2O_4^{2-}$ (1500 cm^{-1}) appears between the D band and G band after discharge.[24] Meanwhile, there is no signal of amorphous carbon on the discharged carbon-free Ni@Ru cathode, suggesting that MgC_2O_4 is the only discharge product. The reversibility of MgC_2O_4 after recharging could be embodied through the observed weakened peaks (Figure 2d). The similar evolution of C=O, C–O, Mg–O vibration bands belonging to MgC_2O_4 could be also observed in Fourier transform infrared (FTIR) spectra (Figure 2e).[25] Furthermore, the X-Ray photoelectron spectroscopy (XPS) peaks assigned to $C_2O_4^{2-}$ (289.1 eV in C 1s, 532.9 eV in O 1s) along with divalent Mg^{2+} (51.3 eV in Mg 2p) also confirm the formation and decomposition of MgC_2O_4 product during discharging and charging (Figure 2f, g and Figure S10).[26]

Taking all the results together, the cathodic pathway in Mg–CO_2 battery with PDA mediation is reversible and can be proposed as $Mg + CO_2 \leftrightarrow MgC_2O_4$. Online CO_2 evolution test was conducted to further verify this reaction (Figure 2h). During the recharge process, the voltage of the pre-discharged Mg–CO_2 battery remains at around 2.3 V (green line), the recorded CO_2 evolution amount, calculated by the formula CO_2 content $(ppm) = n(CO_2)/[n(CO_2) + n(Ar)]$, accumulates with time (red line) and is close to the theoretical value (grey dots). The results suggest that, instead of $MgCO_3$ with wide band gap and high thermodynamic stability requiring a high decomposition energy, more conductive and easily decomposed MgC_2O_4 contributes to the highly reversible cycling of CO_2RR and CO_2ER. PDA serves as the key to the unusual reaction pathway. Whether in the bulk phase of liquid electrolyte or at the interphase of the N-CNT substrate, the strong interaction between PDA and CO_2 would always exist (Figure S11–13, Table S6–8), under which the C=O bond length could be stretched to a large extent and, the inert linear O=C=O bond configuration would twist to nearly ≈122°, closer to O=C=O conformation in MgC_2O_4. Tracing back to its properties, we speculated that PDA, a kind of amine sorbents capturing CO_2 efficiently,[21,22] modified the reactant state of CO_2 and tuned the CO_2RR process through a conversion reaction (NH_2-$(CH_2)_3$–NH_2 + $CO_2 \rightarrow NH_2$-$(CH_2)_2$–CH_2–$NHCOOH$), which was proved by proton nuclear magnetic resonance (NMR) spectra (Figure 2i). Upon introduction of CO_2 in electrolyte
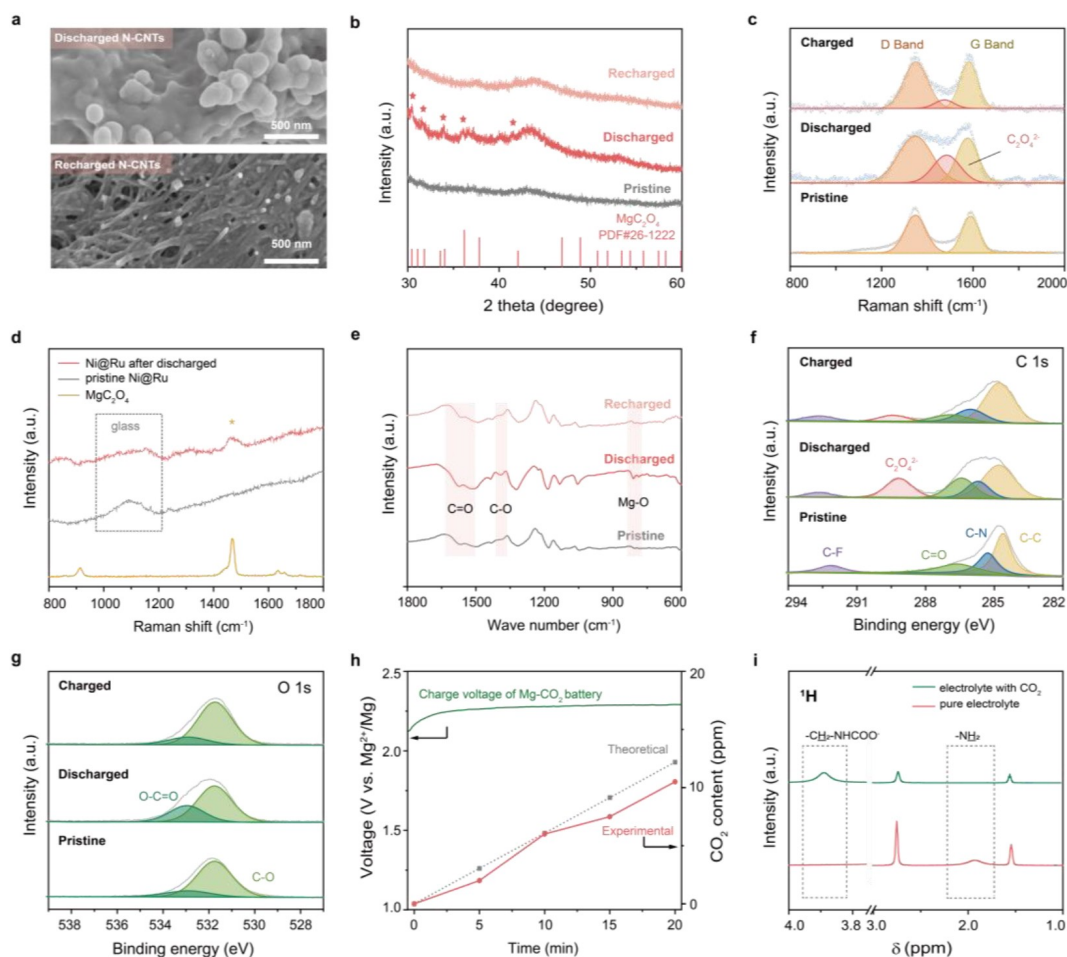
Figure 2. CO_2 capture chemistry and discharge products analysis. a) SEM images of cathodes after discharge and recharge process. b) XRD patterns and c) Raman spectra of cathodes at pristine, discharged and charged states, respectively. d) Raman spectra of the pristine and discharged Ni@Ru cathode. e) FTIR spectra and f, g) XPS spectra of C 1s, O 1s of cathodes at pristine, discharged and charged states, respectively. h) Online CO_2-evolution test and charge voltage of the pre-discharged Mg–CO_2 battery at 100 mA g^{-1} with PDA mediation. i) ^{1}H NMR spectra of 0.25 M Mg(TFSI)$_2$-G4/10%PDA electrolyte before/after CO_2 treatment.

with PDA, the ^{1}H NMR resonance of –NH$_2$, initial observed at 1.9 ppm, disappeared and instead a new peak occurred at 3.9 ppm, representing the formation of carbamic group.[21,27] The formed –CH_2–NHCOO- in liquid electrolyte would be capable of subsequent electrochemical reactions through the easier N–C bond cleavage in place of gaseous CO_2 with the resultant products (MgC_2O_4 mentioned above).

The MgC_2O_4 consisting of only CO_2-derived species also indicate that PDA would meanwhile recover and return to electrolyte for repeatedly CO_2 uptake. This CO_2 capturing chemistry has further been confirmed through the discharging behaviors in pure Ar of assembled batteries after initially stood in CO_2 for 12 h. Bi–Mg anodes rather than pure Mg were used to exclude the influence of passivation issue in baseline electrolyte.[28] With the assistance of PDA in electrolyte, the Mg–CO_2 discharge reaction happened with voltage about 0.75 V, indicating that the absorbed CO_2 to –CH_2–NHCOO- takes part in the electrochemical reaction as active species. While without PDA, the voltage of battery is lower than 0.4 V, which is mainly due to the

capacitive behavior of N-CNT cathode without the CO_2 participation (Figure S14).

Density functional theory (DFT) calculations were adopted to further provide an in-depth understanding of CO_2RR selectivity with PDA involved and identify the origin of optimized cathodic reaction behaviors. Based on previous reports,[10,13,29,30] it is proposed that $MgCO_3$ nucleation in baseline system undergoes pathway I, while MgC_2O_4 nucleation in PDA mediated system is possibly initiated by pathway II and furthermore, hypothetic $MgCO_3$ nucleation with PDA mediation has been listed in pathway II′ for comparison (Figure S15).

We here discuss the reaction thermodynamics through calculated Gibbs free energy change ($\triangle$G) between different intermediates (Figure 3a). In all the pathways, carbonate/oxalate generations accompanied by electron transfer processes are always uphill in the energetic profiles, indicating it proceeds rate-limiting steps. The energy barriers, $\triangle$G, of this controlling step for $MgCO_3$ nucleation in pathway I, MgC_2O_4 nucleation in pathway II, $MgCO_3$
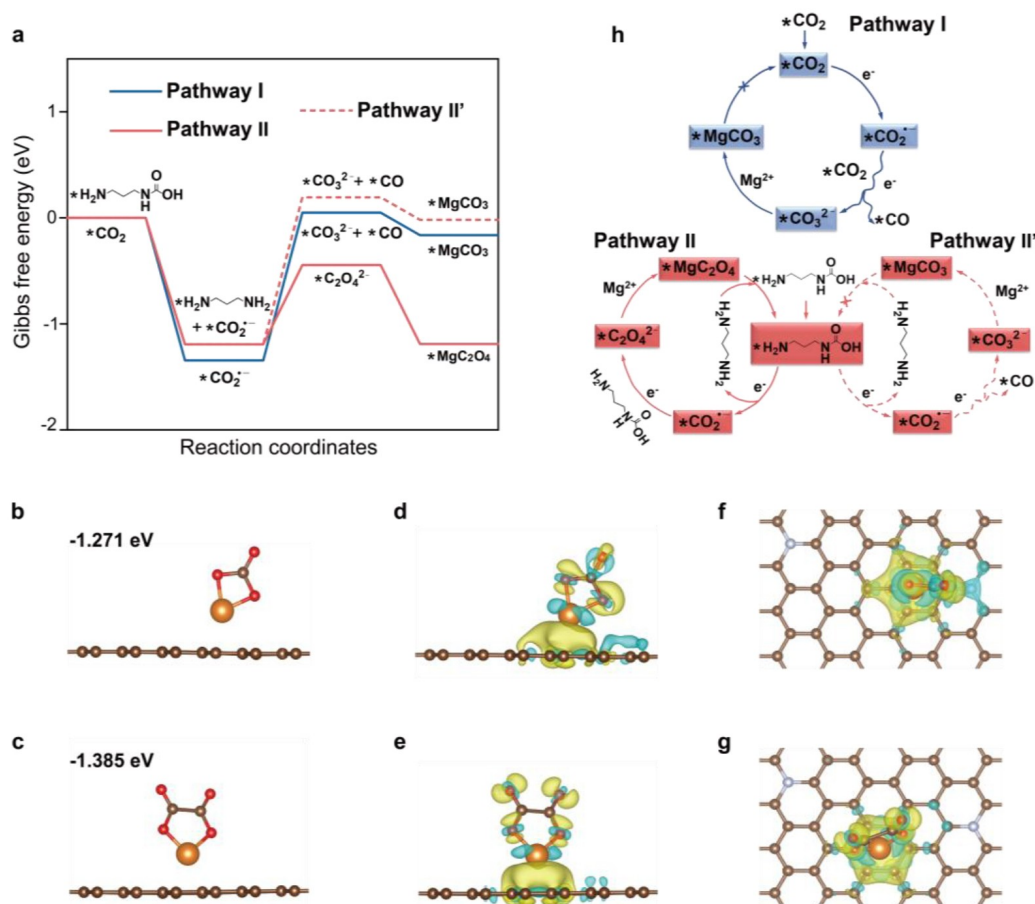
Figure 3. Mechanism of CO_2 conversion chemistry. a) Gibbs free energy change between different intermediates for $MgCO_3$ nucleation in baseline system, MgC_2O_4 and $MgCO_3$ nucleation in PDA mediated system. b) The adsorption of $MgCO_3$ and c) MgC_2O_4 on N-CNT. d, f) The differential charge density upon adsorption of $MgCO_3$ and e, g) MgC_2O_4, the yellow and cyan isosurfaces represent the gain and loss of electron density, respectively from d, e) the side and f, g) top-down views. h) Schemes of reaction process of pathway I, pathway II and pathway II′.

nucleation in pathway II′ are 1.394, 0.748 and 1.386 eV, respectively. To fully overcome the energy barrier, the corresponding applied voltages are calculated to 1.394 V, 0.748 V and 1.386 V in theory (Figure S16). That suggests the electro-reduction of active reactant –CH_2–NHCOO- in PDA tailoring system can be much easier than the sluggish free CO_2 in baseline and more importantly, instead of almost indecomposable $MgCO_3$, more conductive and readily decomposed MgC_2O_4 has been proved to be the thermodynamically favored discharge product in PDA involved reaction pathway.

Adsorption interactions between $MgCO_3$/MgC_2O_4 and N-CNT substrate were further analyzed. Considering the different adsorption modalities, the optimized configurations and energies have been obtained (Figure 3b, c and Figure S17). Obviously, the adsorption of MgC_2O_4 on N-CNT is more preferable with larger negative energy (-1.385 eV) than that of $MgCO_3$ (-1.271 eV). Electron-withdrawing N in N-CNT can stimulate its neighboring C atoms to be active adsorption sites,[31,32] and consistently, the adsorption interactions here mainly derive from the electron donation of N and adjacent C atoms to Mg atoms in adsorbates (Fig-

ure 3d–g). The stronger surface affinity may hinder the MgC_2O_4 molecules aggregation and relieve its subsequent disproportionation reaction.[13] The high energy barrier for MgC_2O_4 splitting to $MgCO_3$ on N-CNT substrate further verify the relative stability of MgC_2O_4 (Figure S18, 19),[11,33] which supports the favorability of MgC_2O_4 as the discharge product, facilitating the reversibility of entire Mg–CO_2 reaction cycle in PDA mediated system (Figure 3h).

Thermodynamic dominance endows the cathode with higher reversibility, while kinetic factors determine the actual reaction rate. In this regard, by pre-incorporating CO_2 into electrolyte with the PDA adduct, the gas-liquid-solid ternary phase reaction at cathode side can be transformed into liquid-solid two phase. The face-to-face interface overcomes the incompatibility and large resistance in ternary phase reactions therefore,[18,34] significantly enhancing the kinetics of CO_2ER and CO_2RR.

As analyzed above, PDA mainly acts as a catalytic mediation for cathodic reaction and remains in electrolyte solution. Therefore, Mg^{2+} solvation environment, may get changed due to the introduced PDA and this will affect the reaction kinetics.

Electrostatic potential (ESP) mapping implies the electronegativity of nitrogen atoms in PDA is a bit stronger than that of oxygen atoms in G4 and thus, PDA could theoretically partially displace G4 to coordinate with electron-withdrawing Mg^{2+} and soften the restriction between G4 and Mg^{2+} (Figure 4a). The interaction between residual PDA and pristine electrolyte have been probed by NMR analysis of various solution compositions. In contrast with the pure G4 (I), the ^{13}C signal of methyl carbon (–CH_3) in G4 shifts down-field in the presence of $Mg(TFSI)_2$ (II), revealing the formation of stable Mg^{2+}–G4 coordination solvation structure.[35,36] When incremental amounts of PDA were introduced (III–V), the relative signals move to up-field in reverse, and gradually close to pure solvent state (Figure 4b). The correlative ^1H spectra also display the similar tendency (Figure S20), indicating that PDA weakens
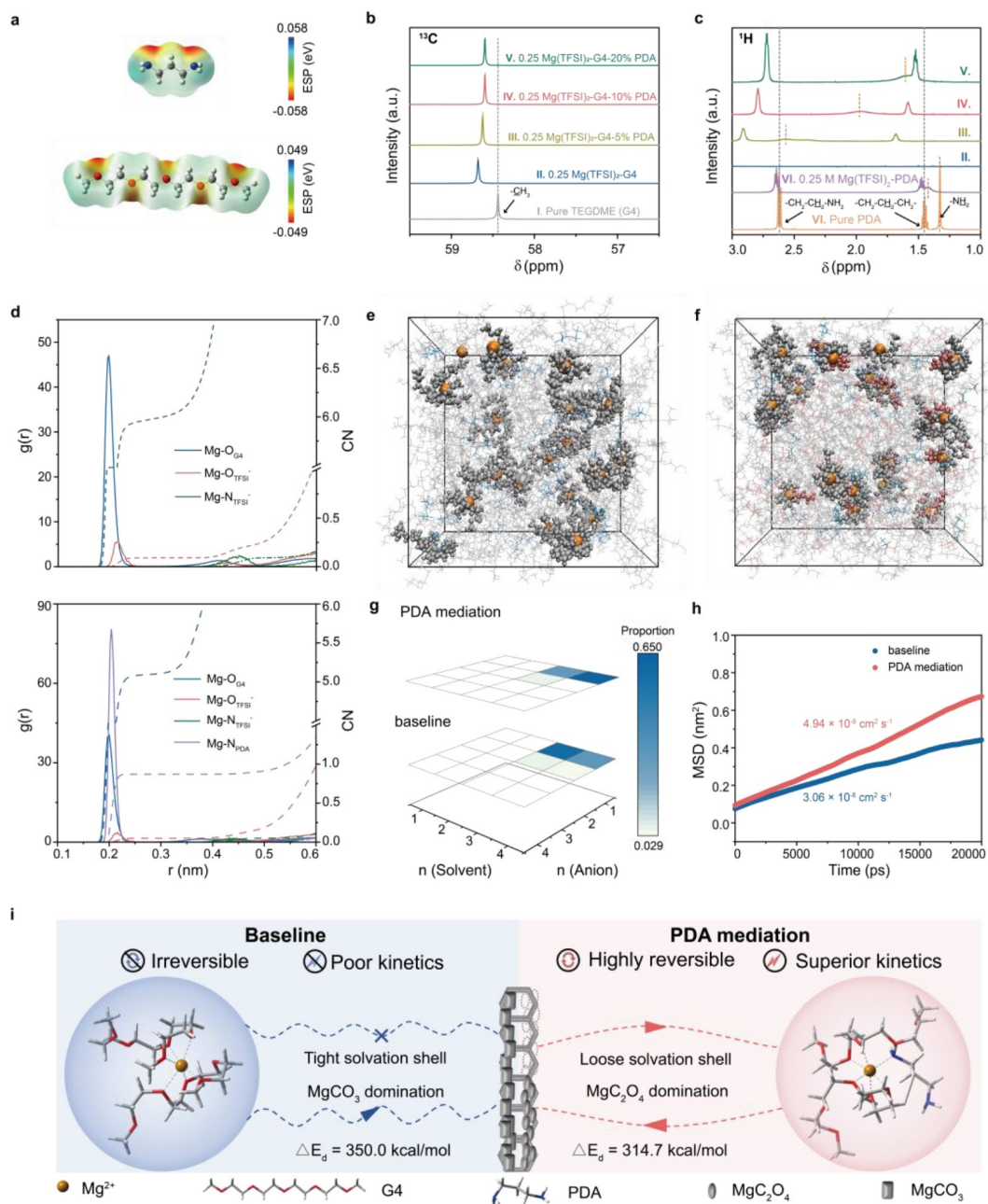

Figure 4. Solvation coordination of Mg^{2+} with PDA modification. a) Electrostatic potential of G4 and PDA. b) ^{13}C NMR spectra of pure G4 and electrolyte with/without PDA. c) ^1H NMR spectra of pure PDA, $Mg(TFSI)_2$-PDA and electrolyte with/without PDA. d) RDF and CN of $TFSI^-$, G4 and PDA in baseline and PDA mediated electrolytes. e) Snapshots of baseline electrolyte and f) PDA mediated electrolyte captured from MD trajectories. Mg^{2+}, $TFSI^-$, G4 and PDA were colored in brown, blue, gray and red, respectively, with the Mg^{2+} solvation structures highlighted using the ball-and-stick model. g) The distribution of Mg^{2+} solvation clusters in different electrolytes. h) Mg^{2+} self-diffusion coefficients from MD simulations. i) Schematic illustration of Mg^{2+}-solvation structure and corresponding features.

the coordination between Mg^{2+} and G4 solvent molecule. The ^1H NMR resonances belonging to PDA likewise illustrate the interaction (Figure 4c). Broader ^1H signal with down-field chemical shift can be observed in 0.25 M Mg-$(TFSI)_2$-PDA (VII) compared to pure PDA (VI), implying PDA is prone to coordinate with Mg^{2+}. For the electrolyte with PDA (III–V), the changes in ^1H NMR resonances of $-NH_2$ protons are more pronounced, that is, the electron density and shielding effect of nitrogen atoms in PDA decrease,[27] in which the coordination with Mg^{2+} mainly occurs and therefore, the original Mg^{2+} solvation coordination has been changed. Raman spectra also reflect the solvation sheath structure change with PDA additive in electrolytes (Figure S21). The broad band around 870 cm^{-1} is associated with C–O stretching and CH_2 rocking modes in free G4 solvent (I), while the newly appeared bands at 560 and 895 cm^{-1} with $Mg(TFSI)_2$ existence are attributed to Mg^{2+}–G4 complex (II).[37,38] With the increasing amount of PDA in electrolyte, the two peaks reveal red-shift or even disappearance (gray line b and c), suggesting the weaker interaction between Mg^{2+} and G4.[39] The enhanced coordination of Mg^{2+} with PDA could be validated through blue-shift of NH_2 bands at about 420 and 940 cm^{-1} (gray line a and d).[40]

Molecular dynamics (MD) simulations were performed to explore the solvation structures in detail. The radial distribution functions (RDF) and coordination numbers (CN) of anions or solvents were calculated. As shown in Figure 4d, baseline and PDA mediated electrolytes both display negligible anions coordination, evidenced by the low CN values of $Mg–O_{TFSI^-}$ and $Mg–N_{TFSI^-}$. The RDF of $Mg–O_{G4}$ with CN of 6.0 around indicates the aggregated Mg–G4 clusters are the main species in baseline system. After PDA introduced, there is a strong interaction between N_{PDA} and Mg cations, so the CN of $Mg–O_{G4}$ reduces to 5 along with the emerged $Mg–N_{PDA}$ coordination. Thus, in agreement with NMR and Raman results, the main role of PDA in electrolyte is to squeeze G4 partially out of the solvation sheath. Corresponding Mg-oriented aggregates can be observed in the MD snapshots (Figure 4e, f), whose occurring proportions have been counted (Figure 4g, Table S9). It turns out that both electrolytes exhibit the largest number of solvent-dominated solvates, namely $[Mg(G4)_2]^{2+}$ and $[Mg(G4)_2(PDA)_1]^{2+}$ with or without PDA participation. Although the number of involved G4 has not changed, the optimized solvation structures show that PDA breaks its tight chelating effects and soften the coordination interaction between Mg^{2+} and surrounding solvents (Figure S22). Consistent with it, the Mg^{2+} diffusion coefficient fitted by MD, conductivity and Mg^{2+} transfer number have all been increased with PDA mediation, specially, from $3.06×10^{-8}$ to $4.94×10^{-8}$ $cm^2 s^{-1}$, 1.46 to 2.08 $mS cm^{-1}$ and 0.36 to 0.45, respectively (Figure 4h, Figure S23–24). Beyond that, the Mg^{2+} dissociation energy (ΔE_d), which could quantitatively evaluate the de-solvation energy barrier of Mg^{2+}, decreases from 350.0 $kcal mol^{-1}$ to 314.7 $kcal mol^{-1}$ using DFT calculation and, the similar tendency can be also verified by MD simulation (Table S10–11, Figure S25), suggesting that Mg^{2+} is more kinetically favorable to dissociate in PDA-mediated

solvation shell compared to baseline. For the completion of the whole Mg–CO_2 reaction, not only the state of CO_2 that been modified by PDA affects the reaction kinetics, as another reactant, the state of Mg^{2+} also plays an important role. In other word, before accepting the electrons, Mg^{2+} would be dissociated from the cluster containing many solvents or anions. Thus, the regulated loose Mg^{2+} solvation shell is anticipated to facilitate fast charge transfer at cathodic interface and thus improve Mg–CO_2 performances. Combining with the MgC_2O_4 nucleation domination by the modification of CO_2, the high reversibility and superior kinetics of CO_2 redox can be largely guaranteed (Figure 4i).

In addition to cathode, the electrochemical behaviors of anode also affect the whole Mg–CO_2 battery performance. As listed in Figure S2, PDA with appropriate amount alleviates anode passivation, enabling long-term reversible plating/stripping. Solvation structures mentioned above also occupy a dominant place for the improved anode. Bulk tailored Mg^{2+} ion transport surely avails the reduced over-potentials, yet the anode-electrolyte interphase induced by modified solvation shell also accelerates the charge transfer kinetics.

Depth XPS with Ar^+ etching was performed to unveil the evolution of anode interphase. For cycled Mg in PDA-containing electrolyte (Figure 5a–c), a emerged peak at 400.4 eV of N–H group, accompanied by a stronger peak of C–N group at 399.8 eV in N1s, are mainly derived from partial PDA adsorption or reduction on Mg anode.[20,41] The preferential interactions between Mg and PDA mitigate the decomposition of $TFSI^-$ on the Mg surface, as evidenced by the lower ratio of notorious passive and Mg^{2+}conduct-inhibiting components (MgF_2, MgN_x, MgO, $MgCO_3$ and $MgSO_x$)[42,43] than that originated from cycled Mg in baseline electrolyte in N1s, F1s, Mg2p, O1s, C1s and S2p spectra (Figure S26, 27). As a result, the interphase arising from decomposed PDA is rich in organic species (C–C, C–O, C–F, C=O, C–N, N–H) that will be easily etched out and thus, the Mg^0 signal increases evidently after 600s Ar^+ sputtering. Similar with Ca^{2+}-conductive interphase,[44] the organic-enhanced thin layer would facilitate Mg^{2+} diffusion, enabling reversible Mg plating/stripping. In sharp contrast, Mg anode undergoes passive interface mainly imbued with the inorganic $TFSI^-$ decomposition products (Figure 5d–e). Beyond the intrinsic unsurmountable barrier for Mg^{2+} diffusion, anion-derived passivation layer is even thicker proved by the weak exposure of Mg^0 signal within the same etching time, which would elongate the Mg^{2+} migration pathway and exacerbate the anodic kinetics. Further conducted SEM characterizations are consistent with all the results obtained from XPS measurements (Figure S28). Basically, the interphase constructed in the electrolyte mediated by PDA is dominated by organic species, which is more conducive to Mg^{2+} transport than the much thicker interphase containing mainly inorganic passive components formed in PDA-free electrolyte, thus ensuring the reversibility of Mg anode for Mg–CO_2 battery (Figure 5g–h). It has also been illustrated in CV curves (Figure 5i). Compared to negligible current response for the Mg||SS in pristine electrolyte, an additional reduction peak can be observed in
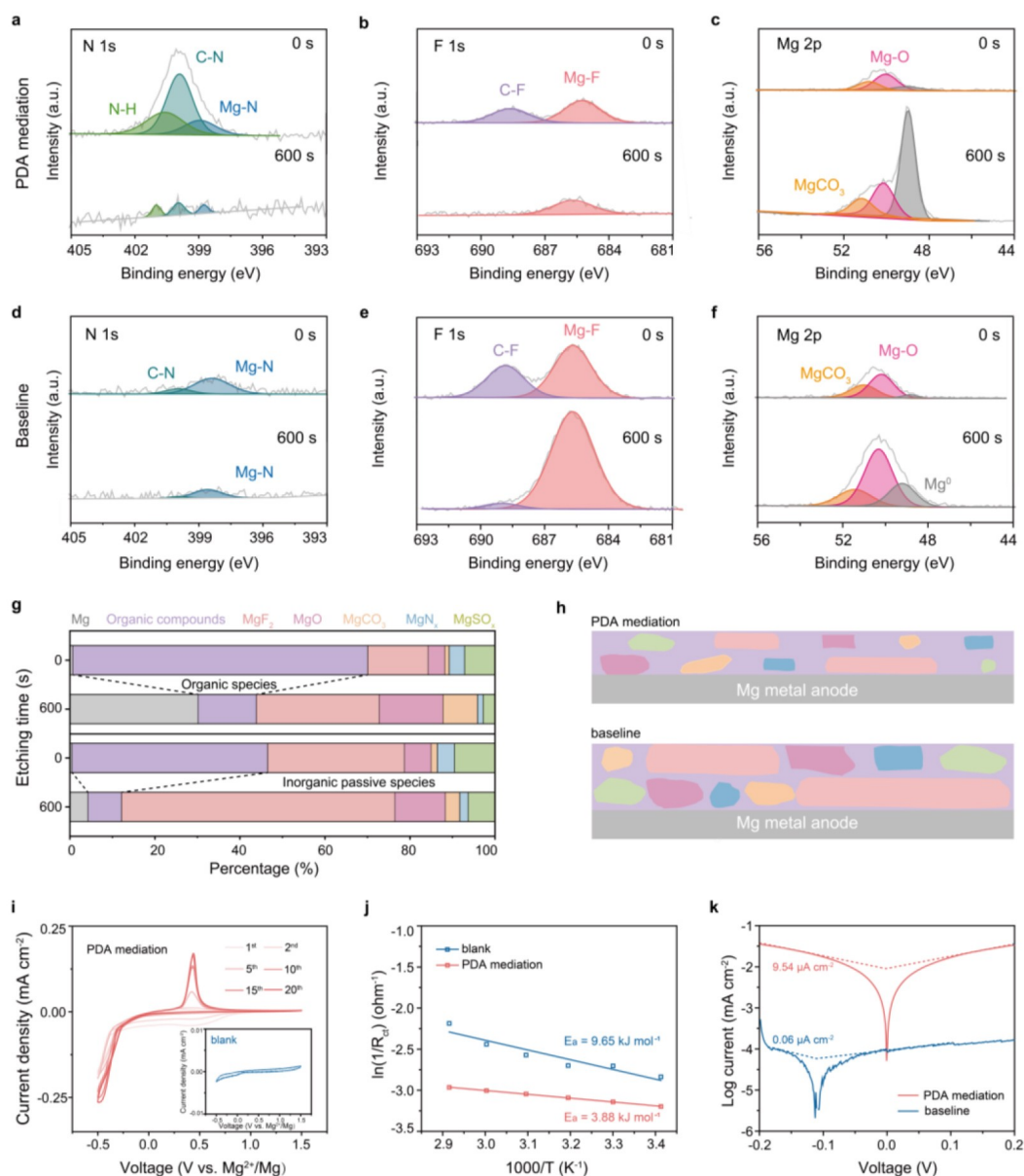
Figure 5. PDA mediated electrolyte for reversible Mg anode interphase. a–c) XPS spectra for N 1s, F 1s and Mg 2p of cycled Mg anodes in electrolyte with PDA and d–f) without PDA before and after 600s Ar$^+$ sputtering. g) The relative proportions of decomposition species and h) corresponding schematic illustrations of cycled Mg anodes in electrolyte with or without PDA. i) CV curves of Mg||SS asymmetric batteries at a scan rate of 5 mV s^{-1} from −0.5 to 1.5 V at different cycles with PDA additive. Inset: corresponding CV curve with blank electrolyte. j) Arrhenius curves and activation energy in two different electrolytes. k) Tafel plots of symmetric cells with or without PDA.

the initial few cycles for that in electrolyte with PDA, apart from a pair of reduction/oxidation peaks related to Mg metal plating/stripping process, suggesting the decomposition of PDA that induces the in situ formation of Mg^{2+} conductive SEI layer on Mg anode. After 10 cycles, the responsive currents gradually keep stable along with only plating/stripping peaks, indicating the complete formation of stable SEI and thus the efficient Mg plating/stripping.

Benefiting from the synergistic effects of favorable electrolyte solvation structure and in situ formed Mg^{2+}-conducting SEI, the significantly enhanced charge transfer

kinetics of anode can be realized. Specially, the calculated activation energy (E_a) has increased by 149 % (from 3.88 kJ mol^{-1} to 9.65 kJ mol^{-1}) with PDA mediation (Figure 5j and Figure S29). The lower impedance (22 kΩ) and higher exchange current density (9.54 μA cm^{-2}) than those of symmetric cells inbaseline electrolyte (537 kΩ, 0.06 μA cm^{-2}, respectively) can be also achieved (Figure 2k, Figure S30). Because of the functions in both electrolyte solvation structure and SEI, the PDA additive boosts the reversibility and kinetics of Mg anodes and consequently the whole Mg–CO$_2$ battery cycling.

Conclusion

In conclusion, amine mediated chemistry strategy has been developed for improving the reversibility and kinetics of both cathode and anode in Mg–CO_2 batteries. Through designing PDA assisted electrolyte, the reactants including CO_2 and Mg^{2+} can be modulated through chemisorption and solvation shell regulation. Therefore, highly reversible and rapid redox conversion of CO_2 and Mg have been realized on thermodynamic-kinetic levels. The PDA-mediated Mg–CO_2 battery delivers excellent cyclic stability for 70 cycles (more than 400 h) with a discharge capacity of 600 mAh g^{-1} under a current density of 200 mA g^{-1} and high-rate performance varied from 100 to 2000 mA g^{-1} with 1.5 V overpotential. Even under low temperature of 0 °C or −15 °C, the system with PDA mediation can still operate normally. This demonstrated strategy provides a feasible scenario to realize a highly rechargeable and high-rate Mg–CO_2 battery, which not only offers effective greenhouse gas utilization, but also provides the promising developments in multivalent metal-CO_2 batteries.

Conflict of Interest

The authors declare no conflict of interest.

Data Availability Statement

The data that support the findings of this study are available from the corresponding author upon reasonable request.

Keywords: Additive Mediation · Carbon Fixation · Electrolyte · Energy Conversion and Storage · Mg–CO_2 Battery

[1] I. Sullivan, A. Goryachev, I. A. Digdaya, X. Li, H. A. Atwater, D. A. Vermaas, C. Xiang, *Nat. Catal.* **2021**, *4*, 952.
[2] F. Wang, Y. Li, X. Xia, W. Cai, Q. Chen, M. Chen, *Adv. Energy Mater.* **2021**, *11*, 2100667.
[3] M. K. Aslam, H. Wang, S. Chen, Q. Li, J. Duan, *Mater. Today Energy* **2023**, *31*, 101196.
[4] H. Wang, D. Yu, C. Kuang, L. Cheng, W. Li, X. Feng, Z. Zhang, X. Zhang, Y. Zhang, *Chem* **2019**, *5*, 313.
[5] K. Wang, Y. Wu, X. Cao, L. Gu, J. Hu, *Adv. Funct. Mater.* **2020**, *30*, 1908965.
[6] W. Ma, X. Liu, C. Li, H. Yin, W. Xi, R. Liu, G. He, X. Zhao, J. Luo, Y. Ding, *Adv. Mater.* **2018**, *30*, 1801152.
[7] W. I. Al Sadat, L. A. Archer, *Sci. Adv.* **2016**, *2*, e1600968.
[8] Y. Liang, H. Dong, D. Aurbach, Y. Yao, *Nat. Energy* **2020**, *5*, 646.
[9] J. Muldoon, C. B. Bucur, T. Gregory, *Chem. Rev.* **2014**, *114*, 11683.
[10] C. Zhang, A. Wang, L. Guo, J. Yi, J. Luo, *Angew. Chem. Int. Ed.* **2022**, *61*, e202200181.
[11] R. Jayan, M. M. Islam, *ACS Appl. Mater. Interfaces* **2023**, *15*, 45895.
[12] M. Mao, T. Gao, S. Hou, C. Wang, *Chem. Soc. Rev.* **2018**, *47*, 8804.
[13] W. Liu, X. Sui, C. Cai, H. Huang, R. Xu, D. Geng, M. Chen, J. Lu, *Adv. Energy Mater.* **2022**, *12*, 2201675.
[14] X. Li, J. Zhou, J. Zhang, M. Li, X. Bi, T. Liu, T. He, J. Cheng, F. Zhang, Y. Li, X. Mu, J. Lu, B. Wang, *Adv. Mater.* **2019**, *31*, 1903852.
[15] S. Yang, Y. Qiao, P. He, Y. Liu, Z. Cheng, J. Zhu, H. Zhou, *Energy Environ. Sci.* **2017**, *10*, 972.
[16] J. Wang, B. Marchetti, X.-D. Zhou, S. Wei, *ACS Energy Lett.* **2023**, *8*, 1818.
[17] T. Shiga, Y. Kato, M. Inoue, Y. Hase, *ACS Sustainable Chem. Eng.* **2019**, *7*, 14280.
[18] X. Sun, X. Mu, W. Zheng, L. Wang, S. Yang, C. Sheng, H. Pan, W. Li, C.-H. Li, P. He, H. Zhou, *Nat. Commun.* **2023**, *14*, 536.
[19] S. Hou, X. Ji, K. Gaskell, P. Wang, L. Wang, J. Xu, R. Sun, O. Borodin, C. Wang, *Science* **2021**, *374*, 172.
[20] F. Wang, H. Hua, D. Wu, J. Li, Y. Xu, X. Nie, X. Zhuang, J. Zeng, J. Zhao, *ACS Energy Lett.* **2023**, *8*, 780.
[21] A. Khurram, M. He, B. M. Gallant, *Joule* **2018**, *2*, 2649.
[22] A. Khurram, L. Yan, Y. Yin, L. Zhao, B. M. Gallant, *J. Phys. Chem. C* **2019**, *123*, 18222.
[23] B. Xu, D. Zhang, S. Chang, M. Hou, C. Peng, D. Xue, B. Yang, Y. Lei, F. Liang, *Cell Rep. Phys. Sci.* **2022**, *3*, 100973.
[24] H. G. M. Edwards, I. R. Lewis, *Spectrochim. Acta Part A* **1994**, *50*, 1891.
[25] M. Sharma, P. Jeevanandam, *J. Alloys Compd.* **2011**, *509*, 7881.
[26] N. Feng, B. Wang, Z. Yu, Y. Gu, L. Xu, J. Ma, Y. Wang, Y. Xia, *ACS Appl. Mater. Interfaces* **2021**, *13*, 7396.
[27] P. V. Kortunov, M. Siskin, L. S. Baugh, D. C. Calabro, *Energy Fuels* **2015**, *29*, 5940.
[28] Y. Zhao, A. Du, S. Dong, F. Jiang, Z. Guo, X. Ge, X. Qu, X. Zhou, G. Cui, *ACS Energy Lett.* **2021**, *6*, 2594.
[29] A. Gennaro, A. A. Isse, M.-G. Severin, E. Vianello, I. Bhugun, J.-M. Savéant, *J. Chem. Soc. Faraday Trans.* **1996**, *92*, 3963.
[30] C. Yang, K. Guo, D. Yuan, J. Cheng, B. Wang, *J. Am. Chem. Soc.* **2020**, *142*, 6983.
[31] Y. Gao, G. Hu, J. Zhong, Z. Shi, Y. Zhu, D. S. Su, J. Wang, X. Bao, D. Ma, *Angew. Chem. Int. Ed.* **2013**, *52*, 2109.
[32] Y. Jing, Z. Zhou, *ACS Catal.* **2015**, *5*, 4309.
[33] R. Jayan, M. M. Islam, *J. Mater. Chem. A* **2023**, *11*, 15915.
[34] C. Zhao, Y. Zhu, Q. Sun, C. Wang, J. Luo, X. Lin, X. Yang, Y. Zhao, R. Li, S. Zhao, H. Huang, L. Zhang, S. Lu, M. Gu, X. Sun, *Angew. Chem. Int. Ed.* **2021**, *60*, 5821.
[35] Y. Shao, T. Liu, G. Li, M. Gu, Z. Nie, M. Engelhard, J. Xiao, D. Lv, C. Wang, J.-G. Zhang, J. Liu, *Sci. Rep.* **2013**, *3*, 3130.
[36] M. Salama, I. Shterenberg, H. Gizbar, N. N. Eliaz, M. Kosa, K. Keinan-Adamsky, M. Afri, L. J. W. Shimon, H. E. Gottlieb, D. T. Major, Y. Gofer, D. Aurbach, *J. Phys. Chem. C* **2016**, *120*, 19586.
[37] T. Watkins, D. A. Buttry, *J. Phys. Chem. B* **2015**, *119*, 7003.
[38] X. He, Y. Ni, Y. Hou, Y. Lu, S. Jin, H. Li, Z. Yan, K. Zhang, J. Chen, *Angew. Chem. Int. Ed.* **2021**, *60*, 22672.
[39] M. Salama, I. Shterenberg, L. J. W. Shimon, K. Keinan-Adamsky, M. Afri, Y. Gofer, D. Aurbach, *J. Phys. Chem. C* **2017**, *121*, 24909.

[40] M. Vogt, C. Pasel, D. Bathen, *Energy Procedia* **2011**, *4*, 1520.

[41] Y. Sun, Q. Zou, W. Wang, Y.-C. Lu, *ACS Energy Lett.* **2021**, *6*, 3607.

[42] R. Attias, M. Salama, B. Hirsch, Y. Goffer, D. Aurbach, *Joule* **2019**, *3*, 27.

[43] Y. Sun, F. Ai, Y. Lu, *Small* **2022**, *18*, 2200009.

[44] Z. Hou, R. Zhou, Y. Yao, Z. Min, Z. Lu, Y. Zhu, J.-M. Tarascon, B. Zhang, *Angew. Chem. Int. Ed.* **2022**, *61*, e202214796.